Journal of Geophysical Research: Solid Earth

RESEARCH ARTICLE
10.1029/2018JB016345

Capturing 50 Years of Postseismic Mantle Flow at Nankai Subduction Zone

Kaj M. Johnson[1] and Douglas Tebo[1]

[1]Department of Earth and Atmospheric Sciences, Indiana University, Bloomington, IN, USA

Key Points:
- Tide gauge records, leveling data, and GPS-derived velocities are combined to form a postseismic vertical deformation field from 1947 to 2015 in southwest Japan
- Two-dimensional models show that afterslip and mantle flow mechanisms are required to explain the postseismic transient
- Vertical deformation data in southwest Japan unambiguously capture 50 years of postseismic mantle flow

Supporting Information:
- Supporting Information S1

Correspondence to:
K. M. Johnson,
kajjohns@indiana.edu

Citation:
Johnson, K. M., & Tebo, D. (2018). Capturing 50 years of postseismic mantle flow at Nankai subduction zone. *Journal of Geophysical Research: Solid Earth*, *123*, 10,091–10,106. https://doi.org/10.1029/2018JB016345

Received 6 JUL 2018
Accepted 13 OCT 2018
Accepted article online 22 OCT 2018
Published online 8 NOV 2018

Abstract We combine Global Positioning System, leveling, and tide gauge records of vertical motion in southwest Japan spanning postseismic deformation following the 1944 M8.1 Tonankai and 1946 M8.4 Nankai earthquakes. Continuous tide gauge records from 1950 to 2015 are combined with leveling data recorded from 1947 to 1980 and Global Positioning System data beginning in 2003 to estimate the spatiotemporal evolution of the vertical velocity field. The combined field shows postseismic subsidence centered approximately 250 km inland from the trench that steadily decreases in rate from 1947 until about 1995. Postseismic uplift is observed in a 50-km-wide belt along the southeast coastline that rapidly decays and reverses to subsidence by the mid-1960s. Both afterslip and viscoelastic mantle flow mechanisms are required to explain the 50-year postseismic deformation transient. We develop a 2-D postseismic deformation model consisting of a linear Maxwell viscoelastic mantle and an elastic subducting slab and overriding plate. Rate-strengthening afterslip on the subduction interface between 20- and 45-km depth and viscoelastic mantle flow relax imposed coseismic stress. Mantle flow with material relaxation time of 8–15 years (viscosity of order 10^{19} Pa s) is required to fit the data. The inland postseismic subsidence signal is diagnostic of postseismic flow in the mantle wedge. Models with rate-strengthening afterslip in an elastic half-space without mantle flow do not produce inland subsidence. The coastal postseismic uplift is largely driven by afterslip. We conclude that vertical deformation data in southwest Japan unambiguously capture 50 years of postseismic mantle flow.

1. Introduction

It has been recognized since at least the seminal studies of Savage and Prescott (1978) and Thatcher and Rundle (1984) that viscous mantle flow plays an important role in the earthquake cycle by relaxing earthquake-induced stresses slowly over time and reloading the fault ahead of the next earthquake. The traditional model of the earthquake cycle consists of an interseismic period of relatively slow accumulation of elastic strain across the subduction plate interface loaded by deep interface creep and viscous mantle flow, punctuated by large earthquakes and rapid postseismic deformation in the form of accelerated fault creep and viscous flow. Wang et al. (2012) reviewed the viscoelastic earthquake cycle concept and demonstrated that surface deformation rates recorded with geodesy may vary significantly throughout the earthquake cycle depending on the effective viscosity of the mantle. Wang et al. (2012) constructed 3-D viscoelastic cycle models to examine late-cycle deformation in Cascadia about 300 years after the *M*~9 1700 earthquake, early postseismic deformation in Sumatra about a decade after the M9.2 2004 event, and late postseismic deformation patterns in Chile about 60 years after the M9.4 earthquake. They found that the deformation patterns are all consistent with subduction zone viscoelastic cycle models with relatively low effective mantle viscosities of order 10^{19} Pa s. Similar average mantle viscosities of 1–5 × 10^{19} Pa s are inferred from postseismic deformation decades after the 1964 Alaska megathrust earthquake (Suito & Freymueller, 2009) and interseismic deformation along the Peru-North Chile subduction zone (Li et al., 2015). This assertion of low viscosity is particularly important in the context of the earthquake cycle because viscosities of order 10^{19} Pa s correspond with short material relaxation times of order 10 years. If this viscosity is representative of the average mantle viscosity throughout the centuries-long earthquake cycle at some subduction zones, we would expect transient deformation to occur at all times of the earthquake cycle.

It is now well known that a single effective mantle viscosity is insufficient for describing the viscous flow of mantle following large earthquakes. For example, Freed and Bürgmann (2004) established evidence for power law flow in the Mojave desert mantle following the 1992 Landers, California earthquake, and Pollitz et al. (2006) and Hu et al. (2016) showed that postseismic deformation following the 2004 Sumatra-

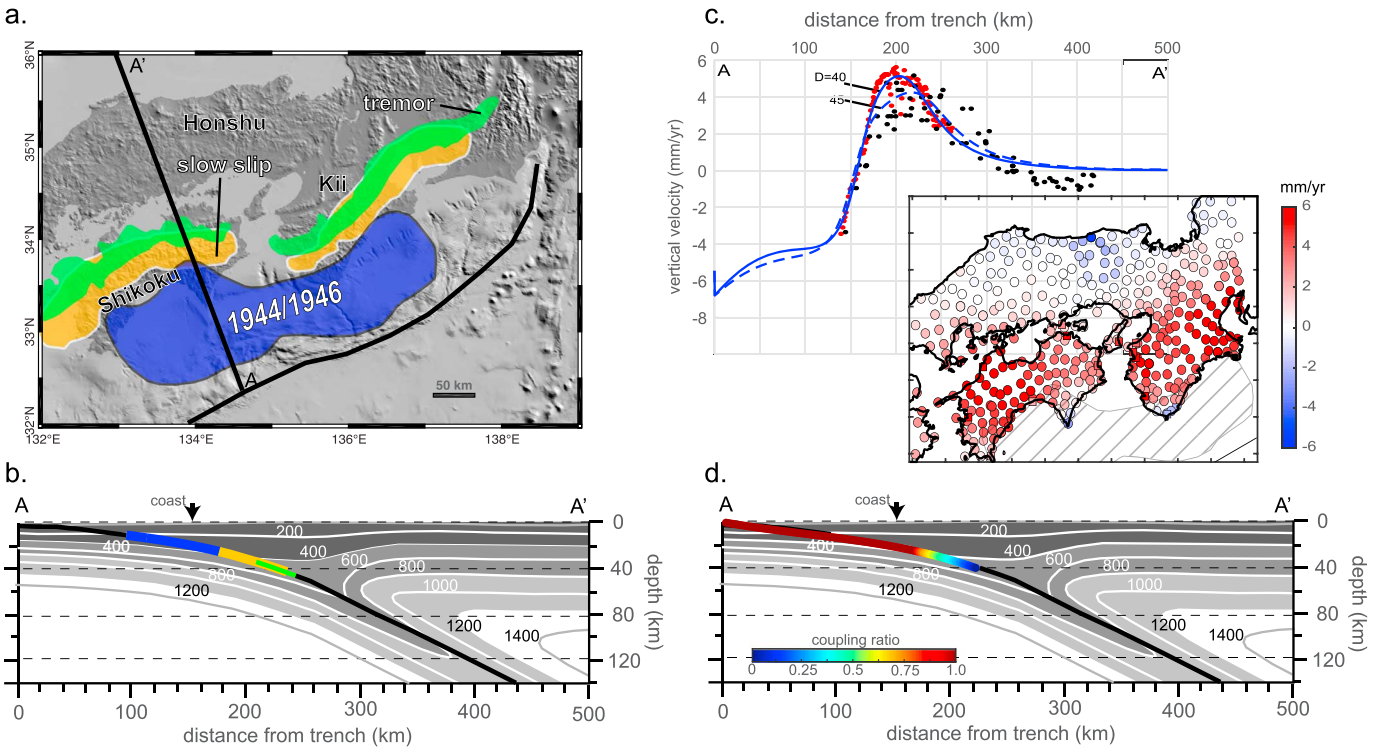

Figure 1. Tectonic setting of Nankai subduction zone region. (a) Map view showing location of trench (heavy black curve), approximate extent of 1944/1946 ruptures (blue; Sagiya & Thatcher, 1999), slow slip (yellow; Nishimura et al., 2013), and tremor (green; Obara & Kato, 2016). (b) Cross-section A-A′ showing computed geotherms from Peacock and Wang 1999 and slip regions using same coloring as in Figure 1a. (c) Present-day (2003–2011) vertical motion rates from GPS data. Profile shows GPS data within 10 km of A-A′ with black circles, and red dots show average rate from leveling data from 1896 to 1934 (Thatcher, 1984). Blue curves show predicted rates from an elastic half-space back slip model with full coupling to 25-km depth and transitional coupling to depth, *D*. (d) Cross section A-A′ showing inferred coupling for elastic back slip model with $D = 40$ (as in Figure 1c). Thermal model same as in Figure 1b. GPS = Global Positioning System.

Andaman and 2011 Tohoku-oki earthquakes, respectively, is best explained with biviscous mantle rheology consisting of a low-viscosity transient contribution. Studies of rapid postseismic deformation within a decade following both the 2004 Sumatra-Andaman and the 2011 Tohoku megathrust earthquakes infer lower average upper mantle viscosities of order 10^{18} Pa s (e.g., Freed et al., 2017; Wiseman et al., 2015). However, it is difficult to infer the effective mantle viscosity at earthquake-cycle timescales of hundreds of years from observations because most geodetic observations of surface deformations have been collected since the mid-1990s, and therefore, our observations at subduction zones span a small portion of the entire earthquake cycle. Southwest Japan (Figure 1) is the only location in the world where we have a geodetic record long enough to potentially capture an entire postseismic phase of the earthquake cycle. Here we have leveling measurements from 1890 to 1980, spanning the 1944 M8.1 Tonankai and the 1946 M8.4 Nankai earthquakes. Tide gauge records since the 1950s can be used to tie together the historical leveling data and the modern Global Positioning System (GPS) records.

Thatcher and Rundle (1984) and Sato and Matsu'ura (1992) modeled the 1890–1980 leveling data in southwest Japan with viscoelastic earthquake cycle models consisting of a rupture on a curved subduction interface in an elastic plate overlying a Maxwell viscoelastic mantle. Both studies concluded that mantle viscosity of order 5×10^{18} Pa s is required to capture the postseismic transients from 1947 to 1980; however, neither model is able to capture all features of the vertical signal. In this paper, we show that these plate models are insufficient for explaining the vertical postseismic deformation because the plate models lack localized flow in the mantle wedge above the elastic subducting slab.

In this study, we tie together leveling, tide gauge, and GPS data to produce a vertical velocity field in southwest Japan spanning nearly 120 years of the earthquake cycle and capturing about 70 years of deformation following the Nankai/Tonankai earthquakes. Newly processed continuous tide gauge records from 1950 to 2015 are combined with leveling data recorded from 1947 to 1980 and GPS data beginning in

2003 with a linear regression approach to estimate the spatiotemporal evolution of the vertical velocity field.

Continuous tide gauge records from 1950 to 2015 are the key to obtaining temporal coverage of postseismic deformation. Our work builds on the work of Savage and Thatcher (1992) who extracted a transient vertical postseismic signal from tide gauge records spanning 1950 to 1985. They were able to identify a decade of transient vertical motions following the Nankai/Tonankai earthquakes up to 1956, but the rates of vertical motion from 1956 to 1985 were not significantly different from a steady rate. However, they recognized that the seemingly steady rate from 1956 to 1985 was inconsistent with the vertical interseismic rate prior to the 1944–1946 earthquakes. There was a hint of a long-lived postseismic transient until 1985 in this data, but as we show here, a longer tide gauge record extending to the present is needed to extract the entire postseismic period.

We also construct a 2-D boundary element model of postseismic deformation consisting of an elastic subducting slab, overriding elastic plate and Maxwell viscoelastic mantle. We show the postseismic vertical velocities along profile A-A′ (Figure 1a) from 1947 to 2017 are explained well with 4 m of imposed slip above 20 km on the interface, rate-strengthening afterslip on the interface between 20- and 45-km depth, and nearly 50 years of viscoelastic mantle flow with an average mantle viscosity of order 10^{19} Pa s.

2. Nankai Setting

Figure 1 shows the tectonic setting of the Nankai subduction zone in southwest Japan. Megathrust earthquakes of magnitude M_w8.1 to 8.4 occur repeatedly at intervals of 100–150 years (e.g., Ishibashi, 2004). The approximate spatial extent of the 1944/1946 Nankai/Tonnankai earthquakes (Sagiya & Thatcher, 1999), shown in Figure 1a, correlates quite closely with the locked portion of the interface inferred from inversions of geodetic data (e.g., Liu et al., 2010; Loveless & Meade, 2010; Yokota et al., 2016; Yoshioka & Matsuoka, 2013). Slow slip occurs both updip and downdip of the locked zone with deep tremor and associated very low frequency earthquakes occurring toward the bottom of the region of deep slow-slip events (e.g., Hirose et al., 2010; Nishimura et al., 2013; Obara, 2010).

The geodetic signal associated with interseismic coupling of the subduction interface is shown in Figure 1c along profile A-A′. Here we show leveling data from 1890 to 1934 from Thatcher (1984) and GPS-derived vertical velocities averaged over 2003 to 2011 (inset, Figure 1c) as explained later in this paper. The vertical velocity profile is explained well with the simple elastic half-space coupling model shown in Figure 1d with the plate interface fully coupled from the trench down to 25-km depth and transitional coupling at constant stress below the locked zone to a depth of 40–45 km (e.g., Bruhat & Segall, 2017). The zone of slow slip and tremor (Figure 1b) is largely within the transitional coupling zone in Figure 1d.

3. Data

3.1. Tide Gauges

We obtained tide gauge data from stations shown in Figure 2 from the Japan Oceanographic Data Center (http://jdoss1.jodc.go.jp/vpage/tide.html). This archive provides hourly tide gauge records beginning from typically 1961 to 1968 and continuing to present day. As discussed below, we also include tide gauge data published by Savage and Thatcher (1992) to extend the records back to 1950.

The time series shown in Figure 2 are constructed in several steps, as illustrated in Figure 3. We first compute a running 2-year mean to remove daily and seasonal trends (Figure 3b). We found similar results with running 1-year and 3-year means. We then remove nontectonic sources of vertical motion in two steps. First, we assume station Sakai is on tectonically stable ground and relative sea level changes at this station are attributed to non-tectonic signals. We subtract the time series at station Sakai from all other time series (Figure 3c). This removes multidecadal trends including the average sea level rise at Sakai from 1965 to 2017 of 2.4 mm/year, which is consistent with the global average over the twentieth century (e.g., Hay et al., 2015). The second step in removing nontectonic signals is to identify and remove common mode noise from all of the stations. We use an empirical orthogonal function approach (EOF) following Savage and Thatcher

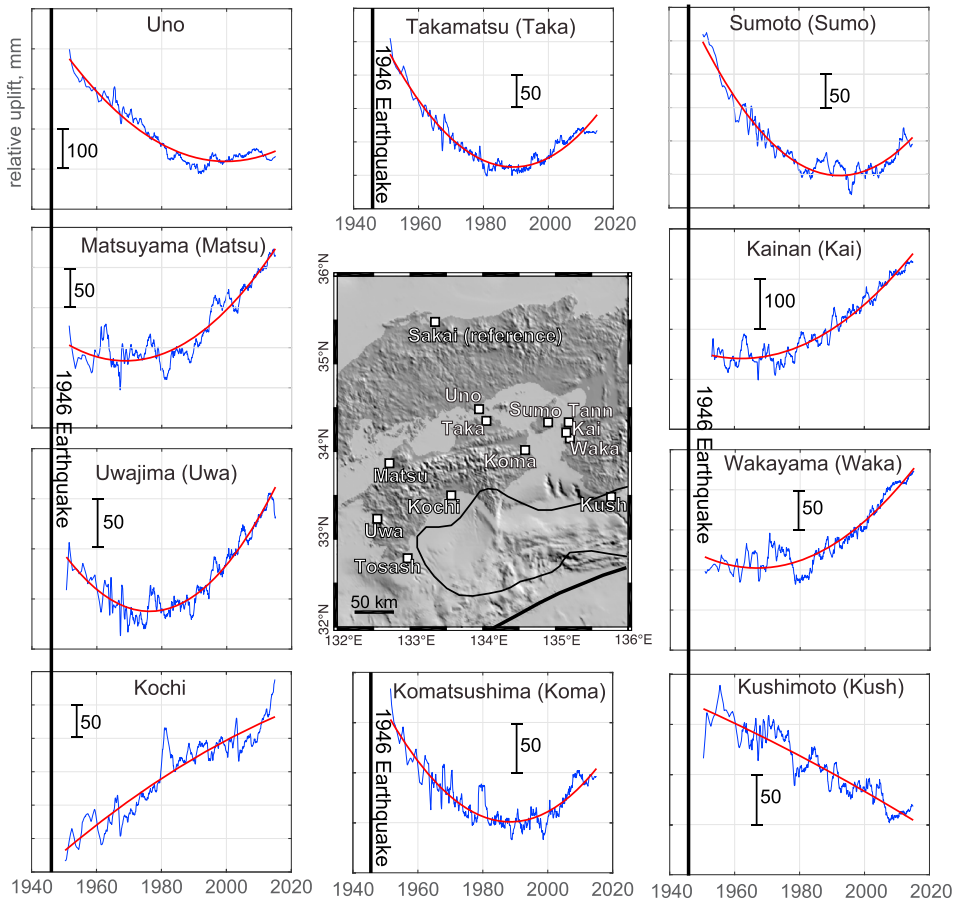

Figure 2. Tide gauge records (blue curves) of land motion relative to Sakai station. Common-mode sea level signal identified from EOF analysis (empirical orthogonal function, i.e., principal components) has been removed. Red curves show the best fitting quadratic curve.

(1992), as illustrated in Figure 4a. We construct a data matrix, $\boldsymbol{Z}$, consisting of tide gauge time series along columns. The singular value decomposition creates a matrix of EOF time series along columns ($\boldsymbol{U}^*\boldsymbol{D}$), and a matrix, $\boldsymbol{V}$, with coefficients for each EOF time series along columns (rows in $\boldsymbol{V}^T$). Figure 4b shows the first EOF time series, and Figure 4c shows the principal components for all 12 tide gauge stations. The first column of the principal components is the coefficients corresponding with the first time series (Figure 4b) in the EOF. The first column coefficients are of similar magnitude and same sign, indicating a common trend in all of the time series. We therefore treat this first time series as common-mode noise and subtract it (scaled by the corresponding coefficients) to produce the final filtered time series as illustrated in Figure 3d. After removal of common-mode noise, multidecadal trends in the time series are evident. Filtered time series and quadratic trends (red curves) of land motion relative to Sakai are shown for 10 stations in Figure 2. supporting information Figure S1 shows all 12 time series before and after removing common-mode noise.

Figure 5 shows snapshots of vertical velocities computed from the quadratic fits shown in Figure 2. We see that that there is a spatially coherent pattern to vertical motions over time, which will become clearer after combining this data set with leveling and GPS data. In particular, inland of the southern coastlines of Shikoku and Kii, widespread postseismic subsidence in 1953, seven years after the 1946 Nankai earthquake, gradually recovers over decades and eventually returns to uplift nearly everywhere by the mid-1990s.

3.2. Leveling

Leveling data from Thatcher (1984) are shown in Figure 6. The leveling data are composed of six lines spanning four time periods from 1890 to 1980. The earliest time period spans 1890/1897 to 1928/1937, with each line having slightly different start and end years. Coseismic displacements are captured with surveys spanning

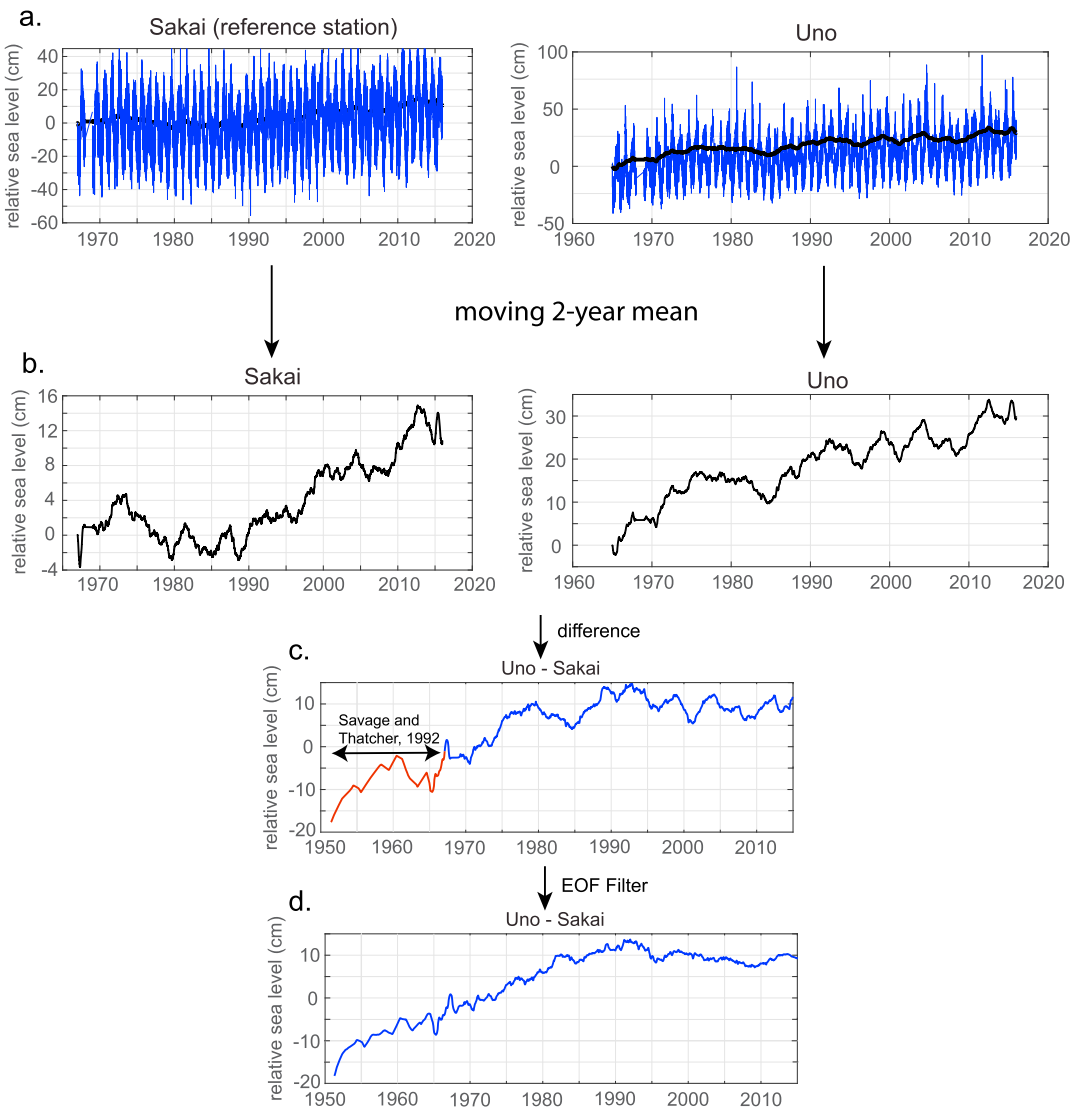

Figure 3. Illustration of time series processing. (a) Hourly data plotted in blue. Moving 2-year mean is shown in black. (b) Time series after applying moving 2-year mean filter. (c) *Uno* time series after subtracting Sakai. Time series is augmented with data from Savage and Thatcher 1992. (d) Final filtered time series after removal of common-mode signal identified with EOF. EOF = empirical orthogonal function.

1929/1942 to 1947. Early postseismic deformation is captured with surveys spanning 1947/1951 to 1964/1967. Later postseismic deformation is captured with surveys spanning 1964/1967 to 1977/1980. We have tied leveling data to the tide gauge rates (Figure 5), by allowing for a vertical shift in relative displacements in leveling, to establish absolute vertical motions for the last two time periods (Figures 6c and 6d).

3.3. Global Positioning System

To compute the vertical GPS velocity field, we use time series from the GEONET F3 solution published by the Geospatial Information Authority of Japan (Nakagawa, 2009). The time series span 2003 to 2011. We remove offsets in the time series using a median filter detection algorithm (Mavrommatis et al., 2014) and fit a straight line to the time series for 2003–2011 to estimate the average rate. We compare these velocities with Median Interannual Difference Adjusted for Skewness (MIDAS) velocities (Blewitt et al., 2016) downloaded from the Nevada Geodetic Laboratory Plug and Play webpage.

Figure 7 shows the vertical velocity using the Geospatial Information Authority of Japan (GSI) data (2003–2011) and the MIDAS velocities (2006–2015). We also show a slightly smoothed version of both

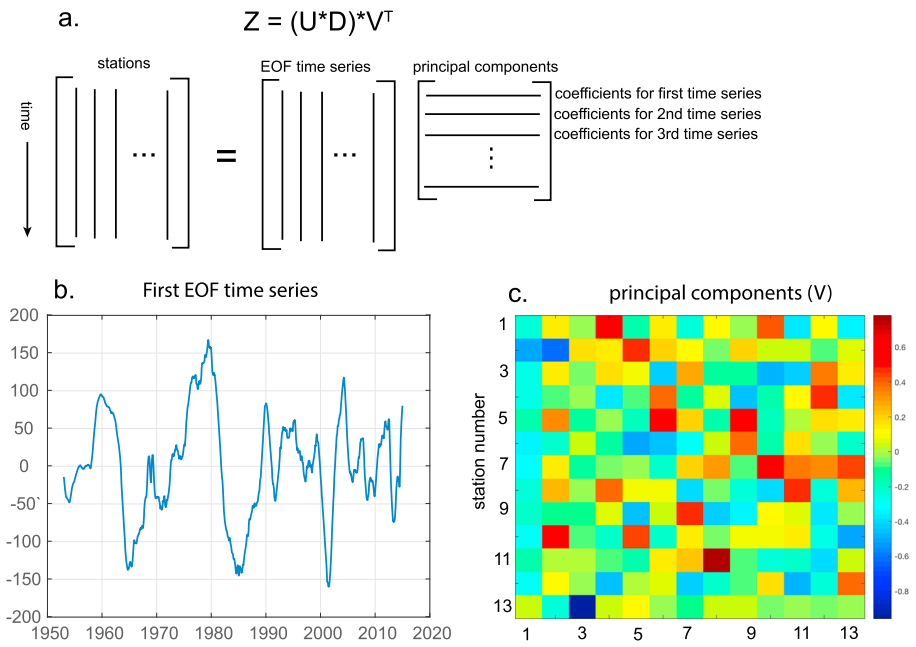

Figure 4. Illustration of empirical orthogonal function (EOF) approach to identifying common mode noise. (a) Singular value decomposition into matrix of columns of EOF time series and matrix of rows of coefficients (principal components) for each time series. (b) Plot of first EOF time series. (c) Principal components. The first column of principal components, corresponding with the first time series, is of similar magnitude and same sign, suggesting common mode.

fields after applying a spatial median filter (e.g., Hammond et al., 2016). We see in Figure 7 that the two solutions yield similar vertical velocity fields, with the point-by-point difference shown in Figures 7c and 7f. The average velocity of the differenced fields are −0.83 and −0.71 mm/year for the unsmoothed and smoothed fields, respectively, indicating that the GSI vertical velocities are on average nearly 1 mm/year faster (more rapid uplift) than MIDAS velocities. This difference may be attributable to different reference frames. There are some spatially coherent differences in the velocity fields at the level of 1–2 mm/year. It is not clear if these differences can be attributed to the different observation time periods or different processing techniques.

Figure 8 compares the 2003–2011 average vertical rate from GPS data (GSI solutions, no spatial filtering) with average rates from tide gauge stations during the same time period. The tide gauge rates are computed by fitting a straight line to the tide gauge time series for this time period. For the sake of comparison, we show the tide gauge rate (red triangles) along with the four nearest GPS stations (blue open circles). The blue bars show the range in the four nearest velocities, and the blue filled circles show the average. The tide gauge and GPS-derived rates are positively correlated, and the range in GPS rates overlaps the tide gauge rate at 9 of the 12 sites. In the following data combination, we choose to use the spatially filtered GSI velocity field to remove spatial outliers.

3.4. Data Combination

The three geodetic data sets, taken together, span about 120 years, but with variable degrees of spatial and temporal coverage. To tie the data together spatially and temporally, we invert the data for a best fitting, time-varying surface. To avoid the complexity of dealing with an instantaneous coseismic displacement, we use only data following the 1944/1946 earthquakes. We solve for the incremental annual vertical displacements every year from 1947 to 2017 (71 time increments) on a regular grid of 875 cells of uniform displacement and dimension (15.4 × 17.2 km) spanning southwest Japan. The velocity field derived from GPS time series (Figure 7d) is assumed to be constant over the duration of GPS observations, 2003–2017. In all, there are $N = 5425$ observations and $M = 62{,}125$ unknowns. Let $\boldsymbol{u}$ be a $M \times 1$ vector of unknown annual displacements, and let $\boldsymbol{d}$ be a $N \times 1$ vector of observed displacements spanning various time periods. We construct the $\boldsymbol{G}_{N\times M}$ matrix of zeros and ones such that $\boldsymbol{d} = \boldsymbol{G}\boldsymbol{u}$. To smooth the displacement field over space, we introduce the finite-difference second derivative spatial smoothing operator, $\boldsymbol{J}_{875\times 875}$, and the $\boldsymbol{L}_{M\times M}$ block

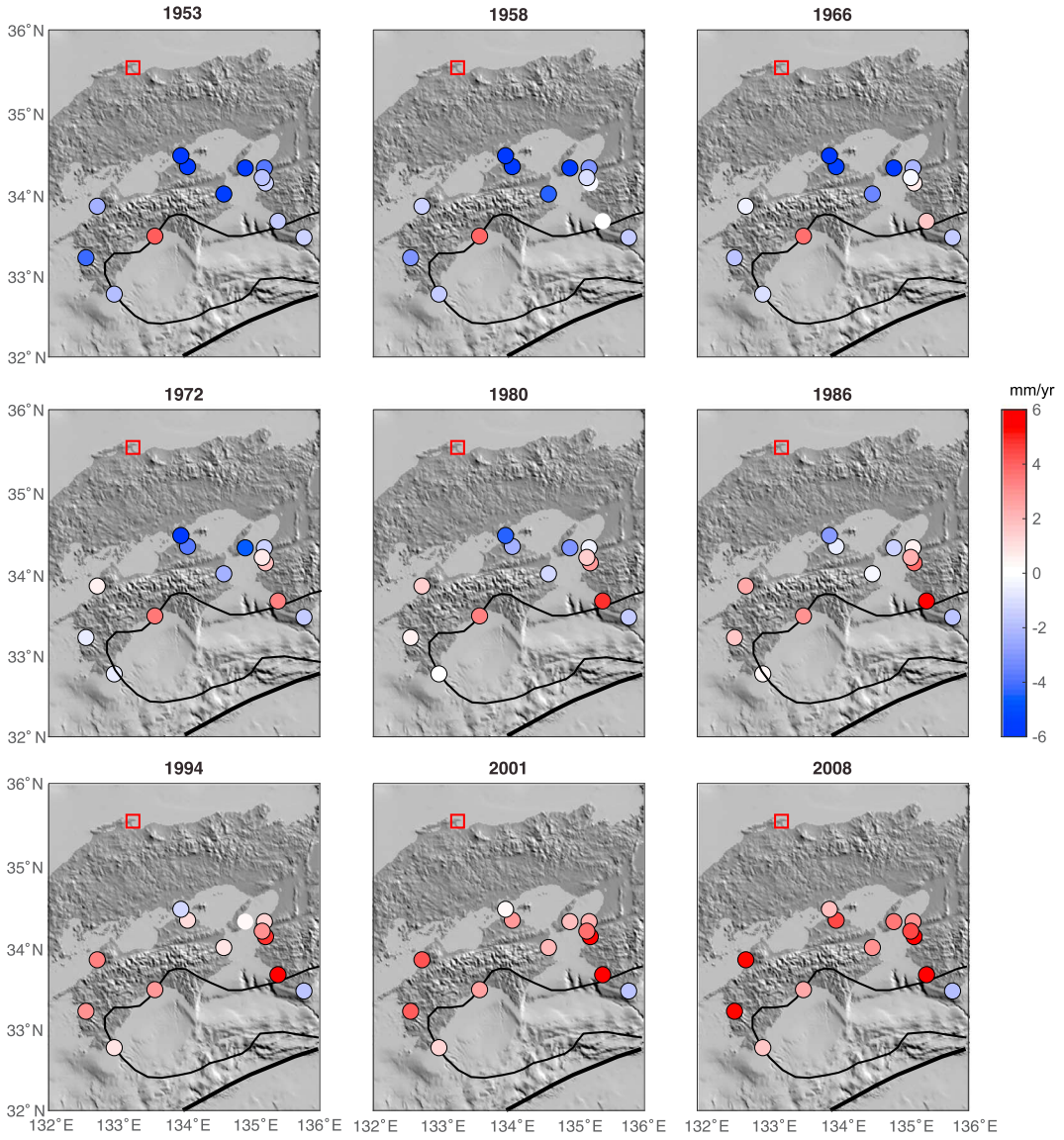

Figure 5. Snapshots of vertical rates of land motion relative to Sakai from tide gauge data. Rates are computed from the quadratic fit to the time series (Figure 2). Red square is reference station, Sakai. Black lines denote trench and coseismic slip region, as in Figure 1a.

diagonal matrix with $\boldsymbol{J}$ on the diagonal. To smooth the displacement field over time, we introduce the sparse matrix, $\boldsymbol{D}_{M\times M}$, containing appropriate placed values of [1–2 1] to impose the second derivative temporal smoothing. We then minimize the objective functional

$$\Phi(u) = [\boldsymbol{d} - \boldsymbol{G}\boldsymbol{u}]^T[\boldsymbol{d} - \boldsymbol{G}\boldsymbol{u}] + \frac{1}{\alpha^2}[\boldsymbol{L}\boldsymbol{u}]^T[\boldsymbol{L}\boldsymbol{u}] + \frac{1}{\beta^2}[\boldsymbol{D}\boldsymbol{u}]^T[\boldsymbol{D}\boldsymbol{u}], \quad (1)$$

where α and β determine the relative weights on smoothing versus fitting the data and are determined subjectively by trial and error such that the surface is not viewed as much smoother or much rougher than the data suggest. The objective functional (1) is minimized using standard least squares and sparse matrix methods in Matlab.

Figure 9 shows snapshots of the velocity field (displacements divided by time increment of 1 year) at selected times. The data are shown with symbols and are plotted at the same color scale as the model surface. The hatched area shows the spatial extent of 1944/1946 rupture. Figure 9a shows rapid uplift along the

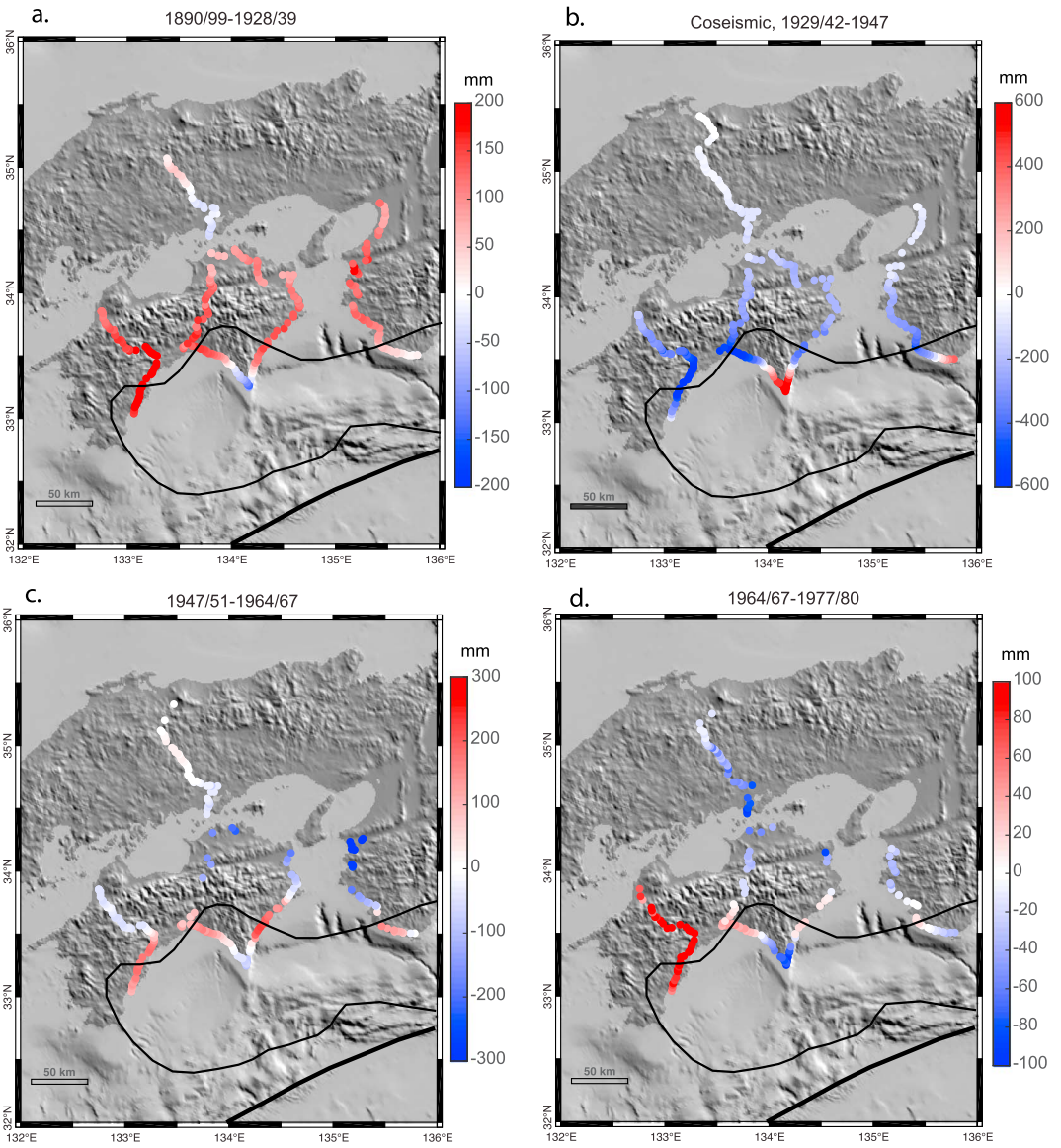

Figure 6. Leveling data from Thatcher (1984). Cumulative displacements during four time periods. Black lines denote trench and coseismic slip region, as in Figure 1a.

southern coastlines of Shikoku and Kii and widespread subsidence inland across the interior seaway between Shikoku and Honshu. The vertical velocities are saturated at ±6 mm/year for ease of viewing, but the subsidence rates exceed 10 mm/year in the early postseismic period. The uplift rate along the southern coastline decays from 6+ mm/year in 1947 to about 1–2 mm/year in 1967 and then gradually increases over time to about 2–4 mm/year in 2014. The rapid inland subsidence decays from greater than 6 mm/year in 1947 to nearly zero in 1977 and then gradually changing into uplift throughout the 1980s on until today. Figure 9b compares the 1890/1897 to 1928/1937 leveling rates with the 2014 model rate. Although not identical, there is generally good agreement with the rates over these two time periods.

To isolate the postseismic vertical signal, we show snapshots of the velocities from 1947 to 1997 after subtracting the 2014 rate in Figure 10. The postseismic transient is effectively over by 1997, as the postseismic velocities are all at or below 1 mm/year, which is well within the uncertainties. Thus, we conclude the postseismic period lasts for approximately 50 years. The decay of inland subsidence over this 50-year time period is evident. The decaying uplift along the southern coastline is evident from 1947 to about 1967, reversing to coastal subsidence by about 1977.

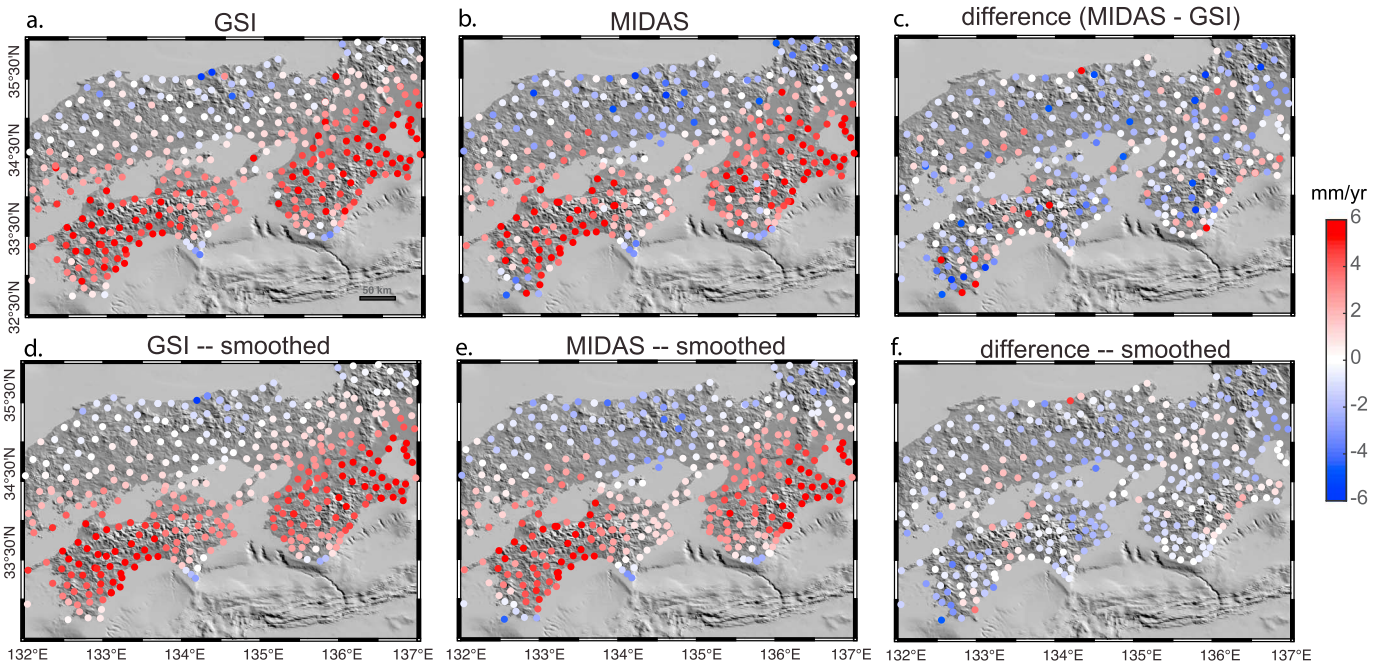

Figure 7. Vertical GPS velocities computed with GSI time series (2003–2011) compared with MIDAS velocities (2006–2017). Top row is the original data. Bottom row is the data after applying a spatial median filter to remove outliers. GPS = Global Positioning System; GSI = Geological Survey Ireland.

4. Postseismic Deformation Model

4.1. Boundary Element Formulation

To model the postseismic deformation field, we construct a 2-D subduction zone model consisting of an elastic overriding plate and elastic subducting slab and a Maxwell viscoelastic mantle, as illustrated in Figure 11. This method is essentially the plane strain version of the method of Huang and Johnson (2012) who developed antiplane strain viscoelastic boundary element models of interseismic strain accumulation across strike-slip faults. Here we only consider postseismic deformation, whereas Huang and Johnson (2012) constructed cycle models.

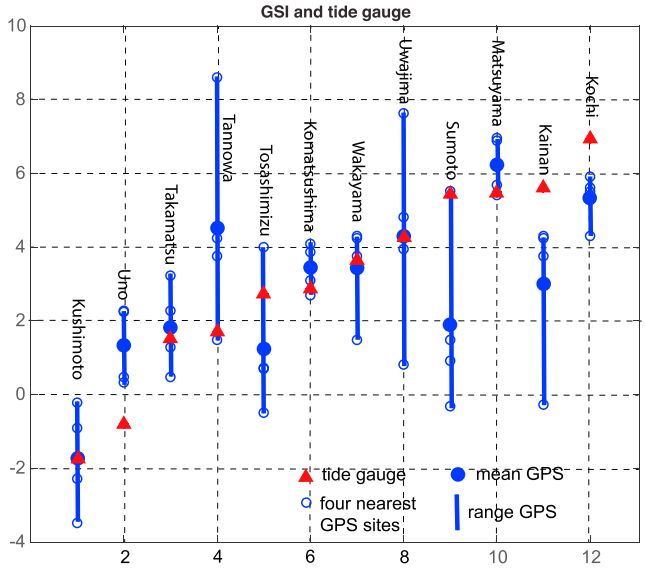

Figure 8. Comparison of tide gauge rates of vertical land motion from 2003 to 2011 and GPS-derived rates (GSI solution, no spatial filter) at the four GPS sites nearest to the tide station. GPS = Global Positioning System; GSI = Geological Survey Ireland.

We build on the elastic displacement discontinuity method of Crouch and Starfield (1982) and discretize surfaces using the solution for plane-strain edge dislocations in an elastic or viscoelastic half-space. The solution for a dislocation in a viscoelastic half-space is easily obtained from the dislocation solution in an elastic half-space using the correspondence principle of viscoelasticity (e.g., Segall, 2010).

We adopt a Maxwell viscoelastic material with governing equation

$$\dot{\sigma}_{ij} + \frac{\mu}{\eta}\left(\sigma_{ij} - \frac{\sigma_{kk}}{3}\delta_{ij}\right) = 2\mu\dot{\epsilon}_{ij} + \lambda\dot{\epsilon}_{kk}\delta_{ij} \tag{2}$$

where λ and μ are the usual elastic Lamé constants, dots denote time derivative, and repeated indices indicate summation. Segall (2010) gives the expression for displacements and stresses for an edge dislocation in an elastic half-space. The detailed expressions are not repeated here as the relationship of displacements and stresses to elastic moduli is the only relevant part of the relationship for this explanation. The stresses are of the form

$$\sigma_{ij} = \frac{\mu}{(1-\nu)} f_{ij} \tag{3}$$

where the f_{ij} are functions of the geometry and dislocation magnitude only

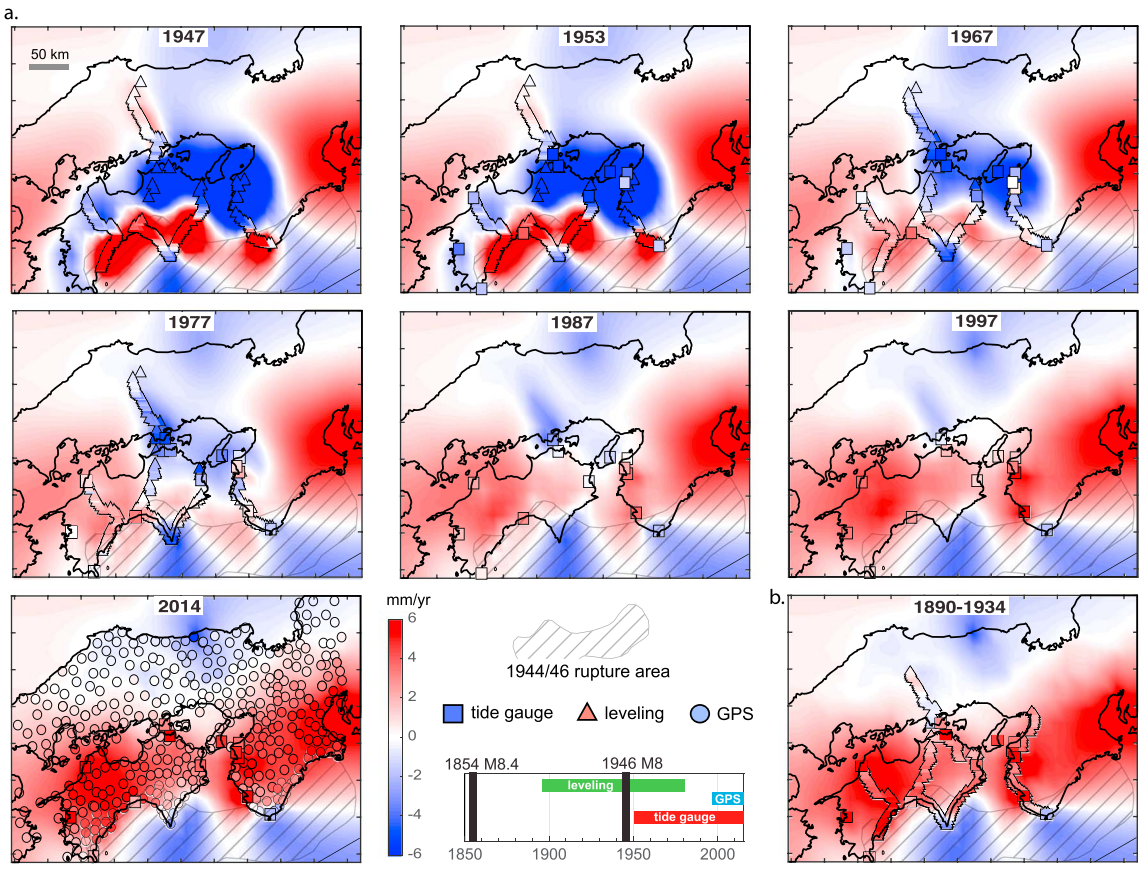

Figure 9. (a) Snapshots of time-space surface fit of all geodetic data. Computed instantaneous vertical rate is plotted at 7 times since the 1946 Nankai earthquake. Surface is fit to data assuming second-derivative smoothing in space and time. Data used to constrain surface are shown with indicated symbols. Timeline shows data coverage. (b) Comparison of 2014 rates (background color) with average leveling rates over 1890–1934 (symbols). Color scale is the same as in Figure 9a.

(not elastic parameters) and v is Poisson's ratio. Thus, applying the correspondence principal of viscoelasticity, the stresses have the simple form in the Laplace domain

$$\overline{\sigma}_{ij}(s) = \frac{\overline{\mu}(s)}{(1-\overline{\nu}(s))} f_{ij} \tag{4}$$

where

$$\overline{\mu}(s) = \frac{\mu s}{s+\mu/\eta}, \overline{\nu}(s) = \frac{1}{2}\ \frac{\lambda s + K\mu/\eta}{(\mu+\lambda)s + K\mu/\eta} \tag{5}$$

and K is elastic bulk modulus. To simplify the inverse Laplace transform, we take the special case of an incompressible elastic material such that $\nu = \frac{1}{2}$. In this case, $\overline{\nu}(s) = \frac{1}{2}$ since $+\lambda = \lambda$. The inverse Laplace transform of stress (4) gives stress in the time domain

$$\sigma_{ij}(t) = e^{-\frac{\mu}{\eta}t} f_{ij}. \tag{6}$$

The stresses simply decay exponentially with characteristic time, η/μ, for the incompressible case. The displacements in an elastic half-space are a function of Poisson's ratio but not μ. Thus, again assuming elastic incompressibility, the displacements in the viscoelastic half-space are independent of time.

Viscoelastic and elastic regions are bounded by straight displacement discontinuity elements as illustrated in Figure 11. The objective of the displacement discontinuity boundary element method is to solve for displacement discontinuity magnitudes subject to matching conditions at contacts between regions, free surface

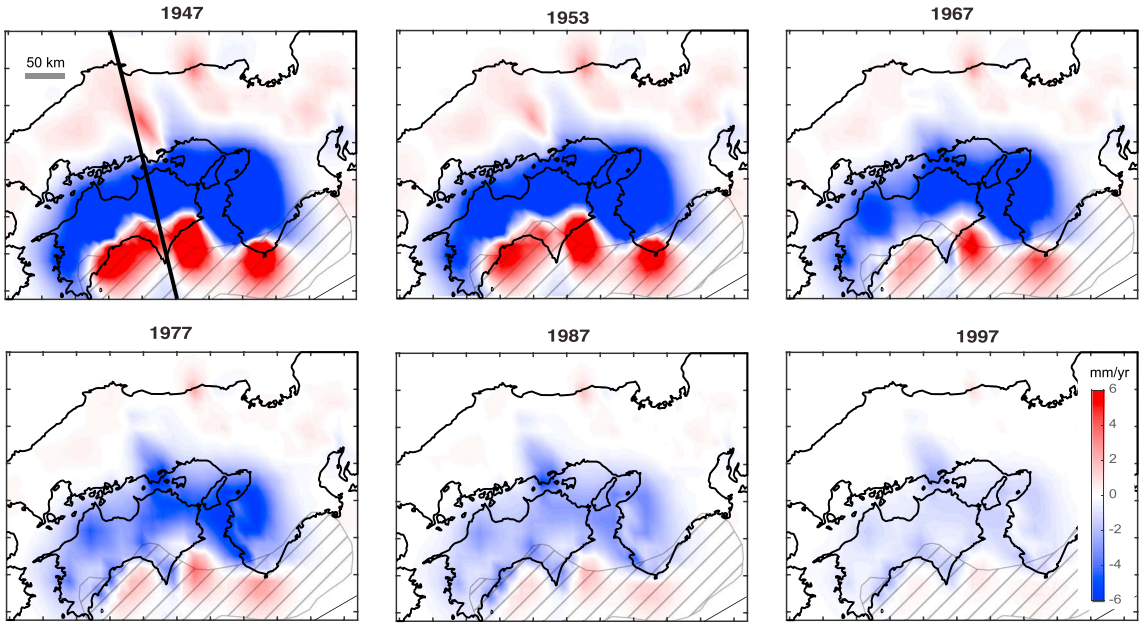

Figure 10. Postseismic deformation. Snapshots of time-space surface fit of all geodetic data after subtracting the present-day rate (2015). Broad region of inland subsidence continues into at least the mid-1990s. Much of the southern Shikoku and Kii coastal areas exhibit rapid postseismic uplift that continues until about 1967. Since about 1967 the entire onland region experiences postseismic subsidence.

conditions, and stress conditions on the subduction interface as shown in Figure 11. We discretize time into Q discrete time steps with logarithmic spacing (shorter time steps immediately after the earthquake), t_k, $k = 0, 1, \ldots, Q-1$. We take $t_0 = 0$ to be the instantaneous time of imposed coseismic displacement. Assume we have an $N \times 1$ vector of incremental values of the two components of displacement discontinuity magnitude (shear and normal) at the jth time increment, $\boldsymbol{s}^j$, on N elements. Suppose P of the N elements forms the creeping portion of the subduction interface (blue in Figure 11). From the solution for a 2-D edge dislocation and solution for decaying stress (6), we can construct the $N \times N$ matrix, $\boldsymbol{G}_s^{j-k}$, and $(N\text{-}P) \times N$ matrix, $\boldsymbol{G}_n^{j-k}$, that relate vectors of shear stresses, σ_s^j, and normal stresses, σ_n^j, at the center of each element during time step j to slip, $\boldsymbol{s}^k$, at time step, k, up to $j-1$

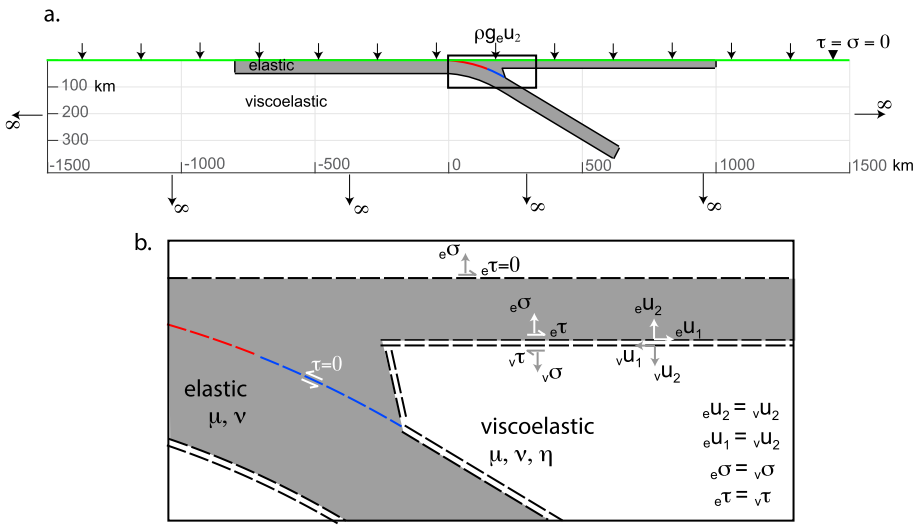

Figure 11. Illustration of boundary element model. a. Elastic overriding plate and subducting slab within viscoelastic medium. Gravitational restoring forces imposed at ground surface. Periodic earthquakes imposed on red portion of interface. Blue portion of interface slips at zero shear stress. b. Enlargement of box shown in a. stress and displacement conditions at boundaries. Viscoelastic and elastic domains are bonded by matching displacements and tractions on boundary elements.

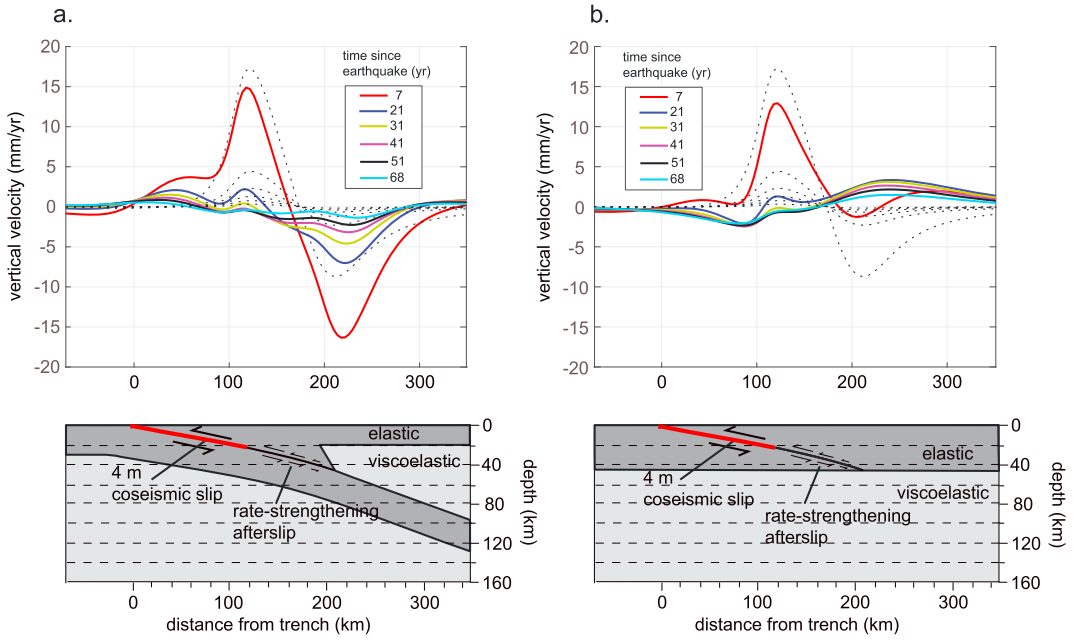

Figure 12. Comparison of vertical velocities predicted by slab (a) and plate (b) models. Color curves show velocities at various times. Dashed black curves show the contribution from only afterslip at the same times. The slab model geometry is identical to the model found to fit the postseismic data. Four meters of coseismic slip is imposed above 20-km depth. Rate-strengthening afterslip occurs below 20-km depth down to the bottom of the elastic wedge at 45-km depth. The plate model interface is identical to the slab model interface. The thickness of the plate is 45 km, which is the depth to the bottom of the elastic wedge in the slab model.

$$\boldsymbol{\sigma}_s^j = \Sigma_{k=0}^{j-1} G_s^{j-k} \boldsymbol{s}^k, \boldsymbol{\sigma}_n^j = \Sigma_{k=0}^{j-1} \boldsymbol{G}_n^{j-k} \boldsymbol{s}^k. \tag{7}$$

At each time step, we require that the traction and displacement matching conditions are met at the interface between elastic and viscoelastic materials as illustrated in Figure 11. We have adopted a notation in Figure 11 where the preceding subscript denotes whether the element is a boundary for the elastic (*e*) or viscoelastic (*v*) medium. We must also satisfy the free-surface condition such that ${}_e\tau = 0$ and ${}_e\sigma - \rho g_e u_2 = 0$ on surface elements. The latter condition approximates gravitational restoring forces where ρ is density of the crust and g is acceleration of gravity (e.g., Segall, 2010). Also, slip rate, v, along the rate strengthening portion of the interface (blue elements in Figure 11) during a time step is determined assuming slip rate is related to shear stress, τ, and normal stress, σ, as

$$\tau = \sigma \left[\mu + (a - b) \ln \left(\frac{v}{v_o} \right) \right] \tag{8}$$

where a-b are the usual rate-state friction parameters and v_o is a reference slip rate. At each time increment, we solve a system of equations for displacement discontinuity magnitudes, $\boldsymbol{s}^j$, by matching boundary and matching conditions as illustrated in Figure 11 and using equations (7) and (8). For the initial condition, we impose uniform slip across the interseismically locked portion of the fault (red surface in Figure 11).

We demonstrate the accuracy of the boundary element solution with a benchmark comparison using a semi-analytical propagator matrix solution for slip on a dipping fault in elastic plate over a linear Maxwell half-space in supporting information (Figure S2).

4.2. Illustration of Model

To illustrate the model predictions of vertical velocities, we compare a subduction zone model with a plate model. The geometries of the models are illustrated in Figure 12. This comparison is particularly appropriate because previous 2-D models of earthquake cycle deformation in southwest Japan adopted a plate geometry like previous studies by Thatcher and Rundle (1984) and Sato and Matsu'ura (1992). Here we use the

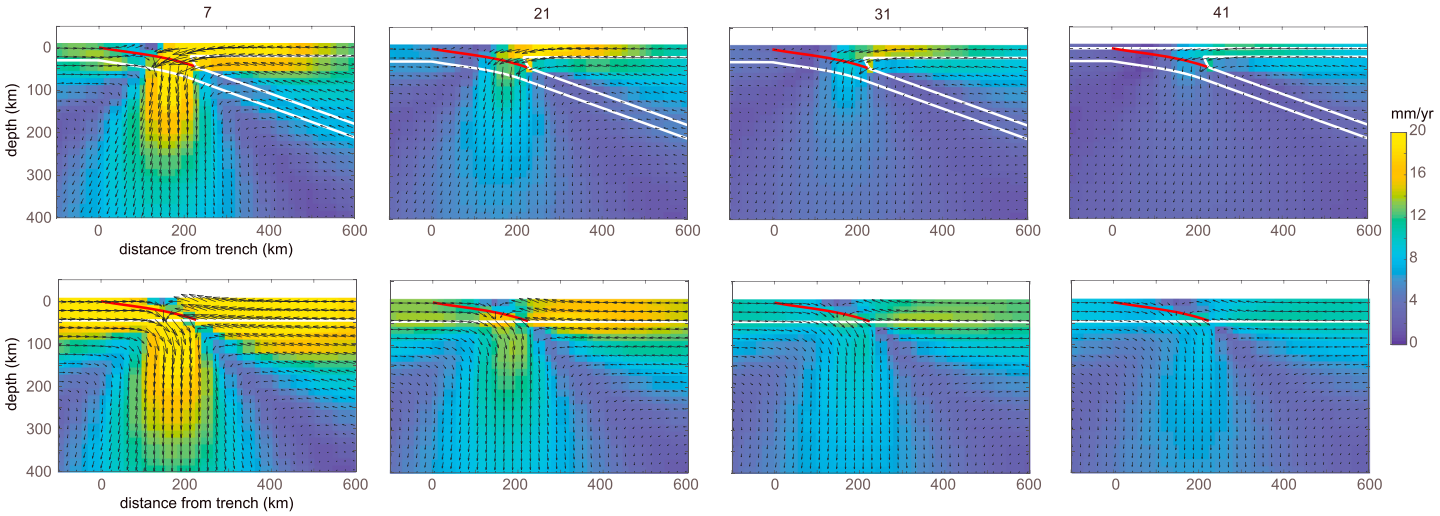

Figure 13. Comparison of velocity fields at depth predicted by slab and plate models in Figure 12. Color shows magnitude of total velocity, and arrows show direction. Color is saturated at 20 mm/year for ease of viewing. White lines show boundaries between elastic and viscoelastic regions. Red line shows slipping subduction interface.

subduction zone geometry that is found to best fit the postseismic observations, as described later in this manuscript. We use the same interface geometry in both models. We impose 4 m of coseismic slip down to a depth of 20 km. Below 20-km depth, afterslip occurs on the interface with σ (a-b) = 0.3 Pa s. The relaxation time, t_r, of the mantle is $t_r = \eta/\mu$ = 10 years. This corresponds with a mantle viscosity of order 10^{19} Pa s. The vertical velocities are computed at the shown times (in years) since the last earthquake in Figure 12. Solid lines are the total postseismic velocity, and the dashed curves show the contribution from only afterslip. It is clear that the predicted vertical velocity profiles are quite different for the two models. In particular, the slab model (Figure 12a) shows postseismic subsidence centered at about 220 km from the trench, above the corner of the mantle wedge. The plate model (Figure 12b), on the other hand, shows uplift at this position.

Figure 13 shows the velocity fields at depth for the two models illustrated in Figure 12. It appears from examination of Figure 13 that the effect of the subducting elastic slab is to localize deformation above the mantle wedge and near the elastic *cold wedge*. This localized deformation is not seen in the plate model. The plate model also produces significantly larger horizontal motions on the downgoing side of the fault.

4.3. Fit to Data

We use a trial and error process to find the geometry and mantle relaxation time that best explain the first-order features of vertical postseismic deformation. We use the United States Geological Survey Slab 1.0 subduction interface geometry (Hayes et al., 2012) to define the model interface geometry above the cold wedge, as illustrated in Figure 14a. The geometry and depth to the bottom corner of the cold wedge and

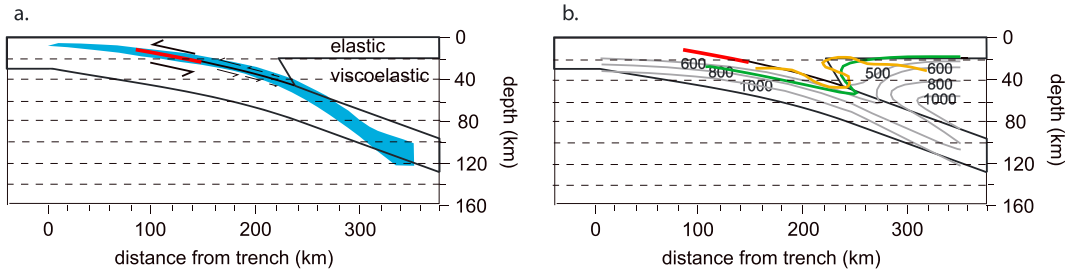

Figure 14. Model geometry showing elastic subducting slab and overrding plate. (a) Uniform coseismic slip is imposed on red portion of subduction interface. Rate-strengthening afterslip occurs below red portion down to bottom of the *cold wedge*. Blue region shows United States Geological Survey Slab 1.0 interface geometry projected onto profile. (b) Comparison of isotherms from thermal models with model geometry. Gray isotherms from Peacock and Wang (1999). Green curve is the 500 °C isotherm from Ji et al. (2016). Orange curve is the 500 °C from Nugraha et al. (2010).

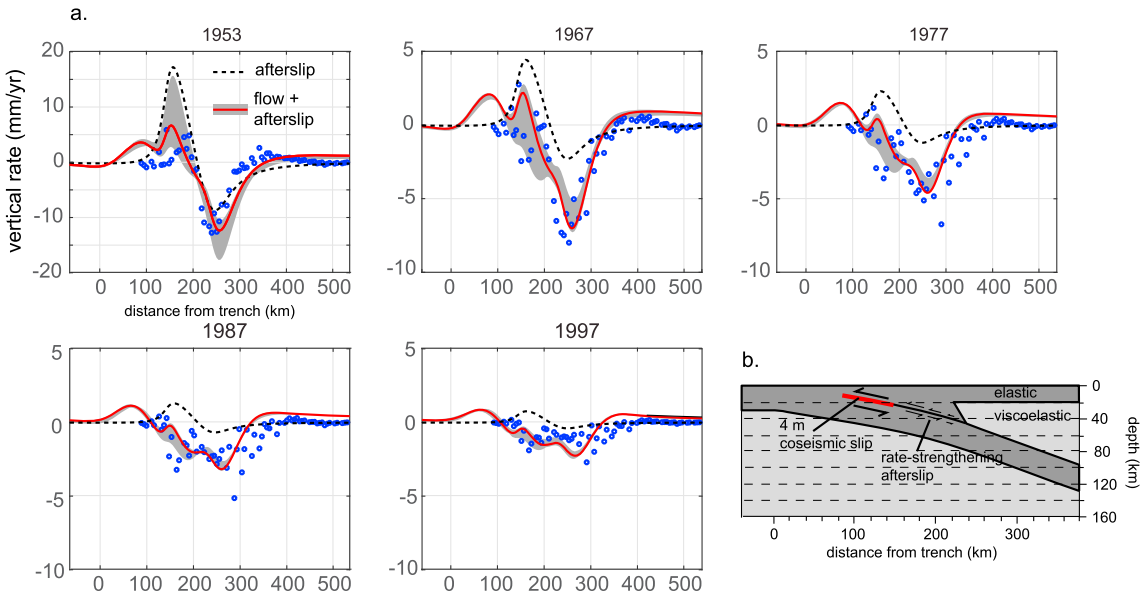

Figure 15. Profiles of data and model predictions. Red line shows the best fitting model, and gray zone shows range of model fits for σ (a-b) ranging from 0.1 to 0.3 Pa and mantle t_r ranging from 8 to 15 years. Dashed black lines show afterslip-only model result. (b) Model geometry. Elastic overriding plate and subducting slab overlying Maxwell viscoelastic crust/mantle. Four meters of coseismic rupture imposed on red section of interface (extending to 20-km depth). Rate-strengthening afterslip is modeled below 20-km depth down to the bottom of elastic wedge at 45-km depth. For best fitting model, relaxation time is 8 years and rate-strengthening friction parameter is σ (a-b) = 0.15 MPa.

the thicknesses of the elastic plate and slab are determined by trial and error. We find that an overriding plate thickness of 20 km and subducting slab thickness of 30 km fits the data best. The bottom corner of the cold wedge is at 45-km depth.

The fit to the data for a range of mantle relaxation times, t_r, of 8 to 15 years and friction parameter, σ (a-b), of 0.1 to 0.3 MPa is shown with gray swaths in Figure 15a at five snapshots in time. The corresponding mantle viscosity for t_r = 8–15 years is 0.8–1.5 × 10^{19} Pa s for typical elastic moduli. The red curve shows velocities for t_r = 10 years and σ (a-b) = 0.15 MPa. The red curve and gray swaths show the total postseismic velocity, and the dashed black curve shows the contribution only from afterslip. It is clear from examination of Figure 15 that uplift near the southern coast in the first 20 years after the earthquake is largely driven by afterslip. Afterslip provides a significant contribution to inland subsidence for the first decade or so after the earthquake, but viscous mantle flow is largely responsible for the continued inland subsidence over the following decades. It is also clear that an afterslip-only model, without mantle flow, is unable to fit the data, because afterslip alone does not produce the sustained inland subsidence.

5. Discussion and Conclusions

Our analysis of geodetic measurements of vertical motion in southwest Japan shows that the postseismic transient following the 1944/1946 M8.1–8.4 Nankai/Tonankai earthquakes continues for about 50 years into the mid-1990s. Rapid postseismic uplift within a ~50-km-wide belt along the southern coasts of Shikoku and Kii decays over about 20 years and reverses to subsidence from 1967 to the mid-1990s. The 2-D postseismic deformation model suggests that this decaying uplift pattern is largely driven by afterslip on the subduction interface. Widespread inland subsidence is observed for about 50 years. The 2-D models show that this widespread subsidence is largely driven by viscous flow in the mantle wedge.

The inferred upper mantle relaxation times of 8–15 years, corresponding with viscosity of order 10^{19} Pa s, is consistent with mantle viscosity in 3-D models by Wang et al. (2012) that reproduce observed variations in the horizontal velocity field throughout the earthquake cycle. Similar viscosities of 1–5 × 10^{19} Pa s are inferred from postseismic deformation decades after the 1964 Alaska megathrust earthquake (Suito & Freymueller, 2009) and interseismic deformation along the Peru-North Chile subduction zone (Li et al., 2015). Studies of

rapid postseismic deformation within a decade following the 2004 Sumatra earthquake and 2011 Tohoku megathrust earthquakes infer lower average upper mantle viscosities of order 10^{18} Pa s (e.g., Freed et al., 2017; Wiseman et al., 2015). These lower viscosities likely reflect transient viscosities that are not representative of the effective upper mantle viscosity inferred over decadal time periods. It is well known that mantle viscosity is strongly stress dependent and therefore rate dependent (e.g., Freed & Bürgmann, 2004). At millennial timescales, and presumably lower deformation rates of the upper mantle, Global Isostatic Adjustment studies infer upper mantle viscosities of order 10^{20}–10^{21} Pa s (e.g., Moucha et al., 2007). We do not have the temporal data coverage in the first decade after the 1944/1946 earthquakes to infer transient mantle viscosity. We are able to fit the observations over 1947–2017 reasonably well with a single Maxwell mantle viscosity.

Figure 14b compares the model geometry with isotherms from several different studies. The gray isotherms are from the kinematic conductive thermal model of Peacock and Wang (1999). The green curve is the 500-°C isotherm from a 3-D thermal convection model by Ji et al. (2016), and the orange curve is the 500-°C isotherm inferred from a seismic attenuation model by Nugraha et al. (2010). The boundary between elastic and viscoelastic domains in our model follows the 500- to 600-°C isotherms remarkably well, suggesting mantle above about 500–600 °C flows throughout the postseismic period, as expected from flow laws for wet pyroxene and olivine (e.g., Bürgmann & Dresen, 2008).

As discussed in Wang et al. (2012), the inferred viscosity of order 10^{19} Pa s has particularly important implications for interseismic deformation and the earthquake cycle at the Nankai subduction zone, and other subduction zones. Interseismic horizontal and vertical deformation is predicted to vary significantly over time for this mantle viscosity, which means that inferences of interseismic coupling at subduction zones using models that neglect mantle flow (i.e., elastic half-space models) might be biased.

Acknowledgments
All data (output model runs) are available in the figures in this manuscript. This work was supported by NSF grant EAR#1620507.

References

Blewitt, G., Kreemer, C., Hammond, W. C., & Gazeaux, J. (2016). MIDAS robust trend estimator for accurate GPS station velocities without step detection. *Journal of Geophysical Research: Solid Earth*, *121*, 2054–2068. https://doi.org/10.1002/2015JB012552

Bruhat, L., & Segall, P. (2017). Deformation rates in northern Cascadia consistent with slow updip propagation of deep interseismic creep. *Geophysical Journal International*, *211*(1), 427–449. https://doi.org/10.1093/gji/ggx317

Bürgmann, R., & Dresen, G. (2008). Rheology of the lower crust and upper mantle: Evidence from rock mechanics, geodesy, and field observations. *Annual Review of Earth and Planetary Sciences*, *36*(1), 531–567. https://doi.org/10.1146/annurev.earth.36.031207.124326

Crouch, S. L., & Starfield, A. M. (1982). *Boundary element methods in solid mechanics: With applications in rock mechanics and geological engineering*. London: Allen & Unwin.

Freed, A. M., & Bürgmann, R. (2004). Evidence of power-law flow in the Mojave desert mantle. *Nature*, *430*(6999), 548–551. https://doi.org/10.1038/nature02784

Freed, A. M., Hashima, A., Becker, T. W., Okaya, D. A., Sato, H., & Hatanaka, Y. (2017). Resolving depth-dependent subduction zone viscosity and afterslip from postseismic displacements following the 2011 Tohoku-oki, Japan earthquake. *Earth and Planetary Science Letters*, *459*, 279–290. https://doi.org/10.1016/j.epsl.2016.11.040

Hammond, W. C., Blewitt, G., & Kreemer, C. (2016). GPS imaging of vertical land motion in California and Nevada: Implications for Sierra Nevada uplift. *Journal of Geophysical Research: Solid Earth*, *121*, 7681–7703. https://doi.org/10.1002/2016JB013458

Hay, C. C., Morrow, E., Kopp, R. E., & Mitrovica, J. X. (2015). Probabilistic reanalysis of twentieth-century sea-level rise. *Nature*, *517*(7535), 481–484. https://doi.org/10.1038/nature14093

Hayes, G. P., Wald, D. J., & Johnson, R. L. (2012). Slab1.0: A three-dimensional model of global subduction zone geometries. *Journal of Geophysical Research*, *117*, B01302. https://doi.org/10.1029/2011JB008524

Hirose, H., Asano, Y., Obara, K., Kimura, T., Matsuzawa, T., Tanaka, S., & Maeda, T. (2010). Slow earthquakes linked along dip in the Nankai subduction zone. *Science*, *330*(6010), 1502–1502. https://doi.org/10.1126/science.1197102

Hu, Y., Bürgmann, R., Uchida, N., Banerjee, P., & Freymueller, J. T. (2016). Stress-driven relaxation of heterogeneous upper mantle and time-dependent afterslip following the 2011 Tohoku earthquake. *Journal of Geophysical Research: Solid Earth*, *121*, 385–411. https://doi.org/10.1002/2015JB012508

Huang, W. J., & Johnson, K. M. (2012). Strain accumulation across strike-slip faults: Investigation of the influence of laterally varying lithospheric properties. *Journal of Geophysical Research*, *117*, B09407. https://doi.org/10.1029/2012JB009424

Ishibashi, K. (2004). Status of historical seismology in Japan. *Annales de Geophysique*, *47*, 339–368.

Ji, Y., Yoshioka, S., & Matsumoto, T. (2016). Three-dimensional numerical modeling of temperature and mantle flow fields associated with subduction of the Philippine sea plate, southwest Japan. *Journal of Geophysical Research: Solid Earth*, *121*, 4458–4482. https://doi.org/10.1002/2016JB012912

Li, S., Moreno, M., Bedford, J., Rosenau, M., & Oncken, O. (2015). Revisiting viscoelastic effects on interseismic deformation and locking degree: A case study of the Peru-North Chile subduction zone. *Journal of Geophysical Research: Solid Earth*, *120*, 4522–4538. https://doi.org/10.1002/2015JB011903

Liu, Z., Owen, S., Dong, D., Lundgren, P., Webb, F., Hetland, E., & Simons, M. (2010). Estimation of interplate coupling in the Nankai trough, Japan using GPS data from 1996 to 2006. *Geophysical Journal International*, *181*(3), 1313–1328.

Loveless, J. P., & Meade, B. J. (2010). Geodetic imaging of plate motions, slip rates, and partitioning of deformation in Japan. *Journal of Geophysical Research*, *115*, B02410. https://doi.org/10.1029/2008JB006248

Mavrommatis, A. P., Segall, P., & Johnson, K. M. (2014). A decadal-scale deformation transient prior to the 2011 M_w 9.0 Tohoku-oki earthquake. *Geophysical Research Letters*, *41*, 4486–4494. https://doi.org/10.1002/2014GL060139

Moucha, R., Forte, A. M., Mitrovica, J. X., & Daradich, A. (2007). Lateral variations in mantle rheology: Implications for convection related surface observables and inferred viscosity models. *Geophysical Journal International*, *169*(1), 113–135. https://doi.org/10.1111/j.1365-246X.2006.03225.x

Nakagawa, H. (2009). Development and validation of GEONET new analysis strategy (version 4). *Geospatial Information Authority of Japan*, *118*, 1–8.

Nishimura, T., Matsuzawa, T., & Obara, K. (2013). Detection of short-term slow slip events along the Nankai trough, southwest Japan, using GNSS data. *Journal of Geophysical Research: Solid Earth*, *118*, 3112–3125. https://doi.org/10.1002/jgrb.50222

Nugraha, A. D., Mori, J., & Ohmi, S. (2010). Thermal structure of the subduction zone in western Japan derived from seismic attenuation data. *Geophysical Research Letters*, *37*, L03303. https://doi.org/10.1029/2009GL041522

Obara, K. (2010). Phenomenology of deep slow earthquake family in southwest Japan: Spatiotemporal characteristics and segmentation. *Journal of Geophysical Research*, *115*, B00A25. https://doi.org/10.1029/2008JB006048

Obara, K., & Kato, A. (2016). Connecting slow earthquakes to huge earthquakes. *Science*, *353*(6296), 253–257. https://doi.org/10.1126/science.aaf1512

Peacock, S. M., & Wang, K. (1999). Seismic consequences of warm versus cool subduction metamorphism: Examples from southwest and northeast Japan. *Science*, *286*(5441), 937–939. https://doi.org/10.1126/science.286.5441.937

Pollitz, F. F., Bürgmann, R., & Banerjee, P. (2006). Post-seismic relaxation following the great 2004 Sumatra-Andaman earthquake on a compressible self-gravitating Earth. *Geophysical Journal International*, *167*(1), 397–420. https://doi.org/10.1111/j.1365-246X.2006.03018.x

Sagiya, T., & Thatcher, W. (1999). Coseismic slip resolution along a plate boundary megathrust: The Nankai trough, southwest Japan. *Journal of Geophysical Research*, *104*(B1), 1111–1129. https://doi.org/10.1029/98JB02644

Sato, T., & Matsu'ura, M. (1992). Cyclic crustal movement, steady uplift of marine terraces, and evolution of the island arc-trench system in southwest Japan. *Geophysical Journal International*, *111*(3), 617–629.

Savage, J. C., & Prescott, W. H. (1978). Asthenosphere readjustment and the earthquake cycle. *Journal of Geophysical Research*, *83*(B7), 3369–3376. https://doi.org/10.1029/JB083iB07p03369

Savage, J. C., & Thatcher, W. (1992). Interseismic deformation at the Nankai trough, Japan, subduction zone. *Journal of Geophysical Research*, *97*(B7), 11,117–11,135. https://doi.org/10.1029/92JB00810

Segall, P. (2010). *Earthquake and volcano deformation*. Princeton, NJ: Princeton University Press. https://doi.org/10.1515/9781400833856

Suito, H., & Freymueller, J. T. (2009). A viscoelastic and afterslip postseismic deformation model for the 1964 Alaska earthquake. *Journal of Geophysical Research*, *114*, B11404. https://doi.org/10.1029/2008JB005954

Thatcher, W. (1984). The earthquake deformation cycle at the Nankai trough, southwest Japan. *Journal of Geophysical Research*, *89*(B5), 3087–3101. https://doi.org/10.1029/JB089iB05p03087

Thatcher, W., & Rundle, J. B. (1984). A viscoelastic coupling model for the cyclic deformation due to periodically repeated earthquakes at subduction zones. *Journal of Geophysical Research*, *89*(B9), 7631–7640. https://doi.org/10.1029/JB089iB09p07631

Wang, K., Hu, Y., & He, J. (2012). Deformation cycles of subduction earthquakes in a viscoelastic Earth. *Nature*, *484*(7394), 327–332. https://doi.org/10.1038/nature11032

Wiseman, K., Bürgmann, R., Freed, A. M., & Banerjee, P. (2015). Viscoelastic relaxation in a heterogeneous Earth following the 2004 Sumatra–Andaman earthquake. *Earth and Planetary Science Letters*, *431*, 308–317. https://doi.org/10.1016/j.epsl.2015.09.024

Yokota, Y., Ishikawa, T., Watanabe, S. I., Tashiro, T., & Asada, A. (2016). Seafloor geodetic constraints on interplate coupling of the Nankai trough megathrust zone. *Nature*, *534*(7607), 374–377. https://doi.org/10.1038/nature17632

Yoshioka, S., & Matsuoka, Y. (2013). Interplate coupling along the Nankai trough, southwest Japan, inferred from inversion analyses of GPS data: Effects of subducting plate geometry and spacing of hypothetical ocean-bottom GPS stations. *Tectonophysics*, *600*, 165–174. https://doi.org/10.1016/j.tecto.2013.01.023